Electroreduction of carbon dioxide to formate at high current densities using tin and tin oxide gas diffusion electrodes

Electroreduction of carbon dioxide to formate at high current densities using tin and tin oxide gas diffusion electrodes

Cite this article as: Sujat Sen, Steven M. Brown, McLain Leonard and Fikile R. Brushett, Electroreduction of carbon dioxide to formate at high current densities using tin and tin oxide gas diffusion electrodes, Journal of Applied Electrochemistry https://doi.org/10.1007/s10800-019-01332-z

Electroreduction of Carbon Dioxide to Formate at High Current Densities Using Tin and Tin Oxide Gas Diffusion Electrodes

Sujat Sen,[1,2] Steven M. Brown,[2] McLain Leonard[2] and Fikile. R. Brushett, [2,*]

[1]Department of Chemistry & Biochemistry, University of Wisconsin-Lacrosse, Lacrosse, WI, 54601, USA

[2]Department of Chemical Engineering, Massachusetts Institute of Technology, Cambridge, MA, 02139, USA

KEYWORDS

electrochemical reduction, carbon dioxide, gas diffusion electrode, flow electrolyzer, formate production, tin oxide

*E-mail: brushett@mit.edu, Phone: 617-324-7400

ORCID

Sujat Sen: 0000-0002-9006-9698

Steven M. Brown: 0000-0002-4360-6286

McLain Leonard: 0000-0003-4572-5251

Fikile R. Brushett: 0000-0002-7361-6637

Abstract

We investigate tin (Sn) and tin oxide (SnO_2) nanoparticle catalysts deposited on gas diffusion layers for the electrochemical reduction of carbon dioxide (CO_2) to formate. The performance and durability of these electrodes was evaluated in a gas-fed electrolysis cell with a flowing liquid electrolyte stream and an integrated reference electrode. The SnO_2 electrodes achieved peak current densities of 385 ± 19 mA cm^{-2} while the Sn electrodes achieved peak current densities of 214 ± 6 mA cm^{-2}, both at a formate selectivity > 70%. The associated peak formate production rates of 7.4 ± 0.6 mmol m^{-2} s^{-1} (Sn) and 14.9 ± 0.8 mmol m^{-2} s^{-1} (SnO_2) were demonstrated for a 1 h electrolysis and compare favorably to prior literature. Post-test analyses reveal chemical and physical changes to both cathodes during electrolysis including oxide reduction at applied potentials less than -0.6 V vs. RHE, nanoparticle aggregation, and catalyst layer erosion. Understanding and mitigating these decay processes is key to extending electrode lifetime without sacrificing formate generation rates or process efficiency.

1. Introduction

The rapidly decreasing cost of wind and solar electricity generation coupled with the growing global consensus on the importance of climate change motivate the decarbonization of the electric power sector and offer exciting opportunities for the electrification of the chemical industry [1-3]. The development of efficient carbon dioxide (CO_2) electroreduction processes, which leverage renewable electrons, would simultaneously curb anthropogenic CO_2 emissions and provide sustainable pathways to create a range of fuels, chemicals, and plastics [4-6]. Recent efforts have focused on the synthesis and characterization of electrocatalysts to convert CO_2 into various products including carbon monoxide (CO), formic acid, methanol, and ethylene [4, 7-12]. Fewer studies have focused on developing reactor configurations that enable these transformations to take place at high production rates and efficiencies [13-15]. A key challenge in the development of a viable electrochemical CO_2 reduction process is transitioning performance nanomaterials to appropriate electrode structures and integrating those electrodes into scalable cell formats, which allow for continuous operation at high current density without sacrificing selectivity or efficiency. Furthermore, the development of instrumented cells that deconvolute the coupled reaction and transport phenomena may facilitate a better understanding of potential- and time-dependent degradation mechanisms, informing design strategies for next-generation materials.

Formic acid or alkali formate salts are attractive CO_2 electroreduction products because they are liquid phase, require only 2 electrons per product molecule, and can be synthesized at high selectivities on a number of non-precious metal catalysts [16, 17]. Formic acid has a range of commercial uses including silage, textiles, leather tanning, pharmaceuticals, crop-protection,

latex processing, and may also find use as a fuel for direct liquid fuel cells [18-20]. While Hori *et al.* initially demonstrated the conversion of CO_2 to formate on several metals (*i.e.*, Hg, Pb, In, Tl, Sn, and Cd) [18], tin (Sn) is arguably the most promising and well-studied catalyst due to its high selectivity, low cost, and lack of toxicity. Building on this work, research has focused on enhancing the activity of Sn catalysts through nanostructuring and/or tuning of the surface chemistry [21-25]. The generation of oxide and oxide-derived surfaces is an emerging approach with recent results demonstrating a maximum current efficiency of > 93% on a 5 nm reduced tin oxide catalyst [26]. The role of the oxide and its stability under electrolysis conditions remains a subject of considerable interest and debate [27-30]. Lee *et al.* demonstrated that the oxide structure of SnO_2 nanoparticles can be maintained over the course of a 5 h electrolysis using the associated Pourbaix diagram to inform the selection of electrode potential and electrolyte pH [31]. Specifically, the authors noted that at pH < 10 and electrode potentials more cathodic than -0.6 V vs. RHE, the metal oxide was partially or completely reduced to metal. However, at pH values of 10 – 12, the oxide phase was found to be stable during electrolysis. This pH range also ensured that the bicarbonate (HCO_3^-) concentration in solution was sufficiently high to act as a proton donor in the proposed CO_2 reduction mechanism. Investigations from Eilert *et al.* have demonstrated the presence of a substantial amount of residual subsurface oxygen in nanostructured oxide-derived copper (Cu) electrocatalysts through a combination of experimental and DFT studies [32]. They attributed the superior catalytic activity to this subsurface oxygen rather than the traditional oxide layer. These findings on Cu may parallel those of Sn. Thus, while the exact role of the oxide layer or subsurface oxygen remains unclear [23], it is evident that metal oxide materials hold promise for CO_2 electrocatalysis.

While significant progress has been made in CO_2 electrocatalysis, most materials are evaluated in electrochemical cells that operate at relatively low current densities (1 – 10 mA cm^{-2}) [33]. In contrast, current densities in the range of 0.5 – 1 A cm^{-2}, which are typical of existing industrial electrochemical processes (*e.g.*, chlor-alkali electrolyzers) [33, 34], are needed to enable cost-effective scaling, but must be realized without sacrificing efficiency. Aqueous-phase CO_2 delivery at ambient conditions (298 K, 1 atm) is hampered by low solubility (33 mM CO_2) and diffusivity (1.91×10^{-5} cm^2 s^{-1}) which, in turn, lead to mass transport limitations that set an upper limit on current density of 10 – 20 mA cm^{-2} [15, 35, 36] . Pressurizing the cell can mitigate mass transfer limitations by increasing the CO_2 solubility, but this approach may lead to additional complexities in cell design, manufacture, and operation [37, 38]. Recently, Hashiba *et al.* demonstrated an electrolysis cell pressurized to 9 atm for converting CO_2 to hydrocarbons on a copper electrode which achieved over 200 mA cm^{-2} with > 50% selectivity to desired hydrocarbon products [39].

Gas phase delivery offers an alternative approach whereby gaseous CO_2 is fed into an electrolysis cell and interfaces with a liquid electrolyte or ion-selective membrane via gas diffusion electrodes (GDEs), which were originally developed as a means of managing gas, liquid, and electron transport at electrochemical interfaces within polymer electrolyte fuel cells (PEFCs) [15]. In this configuration, the high diffusive fluxes of gaseous CO_2 enable increased current densities. Conventionally, a GDE is prepared by depositing an ink consisting of catalyst particles, ionomer, and carrier solvents onto a gas diffusion layer (GDL). The GDL is typically a bi-layer carbon paper or carbon cloth with a denser microporous layer (MPL) that consists of carbon particles and hydrophobic polymer (*e.g.*, polytetrafluoroethylene), onto which the catalyst

is deposited, and a hydrophobized fibrous backing layer, which provides mechanical support, distributes the reactant gas across the catalyst layer, and, in the case of a membrane-based reactor (*e.g.*, PEFC), removes liquid products. While the use of GDEs enables a dramatic increase in current density, typically an order of magnitude or larger, over atmospheric liquid-phase cell designs [40-43], comparatively few studies have focused on catalyst/electrode performance in electrochemical cells with GDEs [14, 43-52]. A brief summary of recent publications that employ gas-phase reactant delivery and Sn-based catalysts can be found in Table S1 (supporting information). Notably, Koplijar *et al.* demonstrated a dry pressing method for the fabrication of Sn GDEs, which were used in a continuous electrochemical cell to reduce CO_2 to formate with a selectivity of > 80% at 200 mA cm^{-2} and an energy efficiency of 22% [45]. Subsequently, the same authors reported SnO_2 GDEs (1.8 wt.% SnO_2 mixed with carbon) which exhibited a formate selectivity of 75% at 400 mA cm^{-2}, a near two-fold performance improvement over the previous Sn GDEs [46]. These studies motivate further investigation into Sn and SnO_2 materials, particularly regarding the impact of catalyst loading and processing on the GDEs. Specifically, achieving lower catalyst loadings without sacrificing performance is desirable because: (1) the thermodynamic driving force to minimize surface free energy and therefore the likelihood of particle agglomeration is reduced, (2) the porous network that facilitates reactant mass transport is less obstructed and may eventually enable even higher reaction rates, and (3) the long-term economic feasibility will increase with decreased materials requirements. Further, examining stability and minimizing the transient behavior of nanostructured catalysts is critical to developing commercially viable materials.

Here, we investigate the performance and durability of Sn and SnO_2 GDEs in a flow-through electrolyzer with gas phase reactant delivery to both electrodes separated by a flowing liquid electrolyte stream that enables product removal from the cell for *ex-situ* quantification. To enable cathode characterization at high current densities *in-operando* and unencumbered by equipment limitations, we integrate a reference electrode into the flowing electrolyte stream and employ the facile hydrogen oxidation reaction on a geometrically larger counter electrode (anode). Performance testing reveals that, for both Sn and SnO_2 cathodes, current densities and faradaic efficiencies of > 200 mA cm^{-2} and > 70%, respectively, are obtained at nominal catalyst loadings of 0.3 mg cm^{-2}. While higher current densities are observed with the SnO_2 electrode, the applied potentials necessary to maximize formate production rates also result in the reduction of the oxide phase. Through pre- and post-test morphological characterization of the electrode, we correlate time-dependent formate current efficiency performance reductions to deleterious evolutions in the catalyst layer during electrolysis. A combination of electrode engineering and careful control of operating conditions may enable extended lifetime without sacrificing performance.

2. Experimental Details

2.1 Preparation of gas diffusion electrodes

Sigracet 39 BC (Fuel Cell Store) gas diffusion layers (GDL) were modified with catalyst and used as the foundation for the gas diffusion electrodes (GDEs) in this study. With a nominal thickness of 325 μm, the GDL consists of a 5 wt% polytetrafluoroethylene (PTFE)-treated carbon paper and a microporous layer (MPL) containing 23 wt% Teflon. The MPL side was

coated with catalyst particles by either air-brushing (cathode catalysts: unsupported Sn nanoparticles, 150 nm diameter, Sigma Aldrich, or SnO_2, < 100 nm diameter, Sigma Aldrich) or hand-painting (anode catalyst: 20 wt.% Pt on Vulcan XC-72, Fuel Cell Store) inks and then air-drying. For all electrodes, catalyst inks were prepared in ratios of 10 mg catalyst, 6.9 μL Nafion ionomer solution (LIQUion 1100 EW, Ion Power Inc., 15% w/w), 400 μL of deionized water (Millipore filtered to 18.2 MΩ), and 400 μL of isopropyl alcohol (99.9% pure, VWR Chemicals) and scaled appropriately based on the number of electrodes being prepared and the desired loading [42]. All inks were sonicated for 20 min to ensure uniform mixing and were either painted or air-brushed (Speedaire airbrush kit, Model #48PX91, Grainger Inc.) onto the MPL of the GDL to create a gas diffusion electrode (GDE) covered with catalyst over a fixed geometric area of 9 cm^2 (3 cm × 3 cm). Typical cathode and anode loadings were 0.35 ± 0.07 mg cm^{-2} and 1.00 ± 0.15 mg cm^{-2}, respectively, which was determined by weighing the samples before and after catalyst application [42]. Each catalyst coated GDE was cut with scissors into smaller pieces to be used in the electrolysis experiments. Directly prior to cell assembly, the anode was hot pressed (Carver Hydraulic Unit Model #3912) together with a Nafion 212 (50 μm thick, Fuel Cell Store) membrane that had been pre-soaked in an aqueous electrolyte consisting of 0.5 M Na_2SO_4 and 0.5 M Na_2CO_3. The membrane and anode were pressed at 120 °C and 50 psi (344 kPa) for 5 min, and then rehydrated in fresh electrolyte (0.5 M Na_2SO_4 and 0.5 M Na_2CO_3) for 1 h prior to experiments.

2.2 Electrochemical Cell Design and Setup

All electrochemical experiments were performed at room temperature in a custom-built small volume flow cell, shown in Figure 1, which was adapted from a previously reported redox flow

battery design [53]. More detailed engineering drawings are provided in the supporting information (Figure S1). All major cell components were fabricated using a CNC mill (Roland DG Corporation, Model A ProII, Rotary Axis Unit, ZCL-540). Both the gas diffuser plates and electrolyte flow channel were machined from acrylic (Optically Clear Cast Acrylic Sheet, 3/4 in. thick, 6 in. × 12 in., McMaster-Carr), which was chemically compatible with aqueous electrolytes used in this study. The electrolyte channel contains a window of 1.5 cm × 1.7 cm (2.55 cm^2) where the electrolyte interfaces with the catalyst layers, which defines the maximum geometric active area for the cell, and a 1/4 in. circular port approximately in the middle of the 0.5-in. thick channel to accommodate a reference electrode (Ag/AgCl, 3 M NaCl, BASi Inc., nominally +210 mV vs. SHE), which enables three-electrode operation. The flow fields, which also serve as current collectors, were machined from 3.18 mm thick impregnated graphite (G347B, MWI, Inc.) with 12 mm × 1 mm rectangular slots for inlet and outlet gas flow such that all the reactants are forced through the porous electrode in a flow-through configuration. The GDEs were sealed into the cell using gaskets cut from 1/16 in. thick, 60A durometer hardness, butyl rubber sheets (McMaster-Carr). To accommodate the current and voltage limits of the potentiostat (VSP-300 Biologic), the active area of the working electrode (cathode) was reduced to 0.5 cm × 0.5 cm (0.25 cm^2) by masking off a portion of the surface with Kapton tape, while the full counter electrode (anode) area was retained (2.55 cm^2), resulting in a cathode to anode ratio of 1 to 10. While this cell configuration is not representative an at scale electrolyzer, it serves as useful electrochemical platform for unambiguous evaluation of different cathode GDEs under operating conditions that approximate practical conditions (e.g., high CO_2 fluxes, high surface area electrodes) without the need for specialized electrochemical equipment. The entire cell was assembled and tightened using a torque screwdriver (Mountz Inc.) with a torque of 14 –

16 lb_f-in (1.6 – 1.8 N-m). Reported potentials are referenced to the Ag/AgCl electrode. To ensure accuracy, before every experiment, the potential of the Ag/AgCl reference electrode was measured against a saturated calomel electrode (Fisher Scientific, nominally +242 mV vs. SHE) dedicated for calibration and not for experiments that could compromise its integrity. The difference in potential was always within ± 20 mV of the expected value. The exact value within that 20 mV range was not recorded and contributes to the experimental uncertainty in all reported electrode potentials. For comparison with other reporting scales, the Ag/AgCl electrode potentials can be converted to the reversible hydrogen electrode (RHE) scale, within ± 20 mV accuracy, via the following equation: E (RHE) = E (Ag/AgCl) + 0.210 + 0.0591 × pH. In this study, the electrolyte pH is 11.36 and assumed to be constant regardless of formate production and minor levels of carbonation.

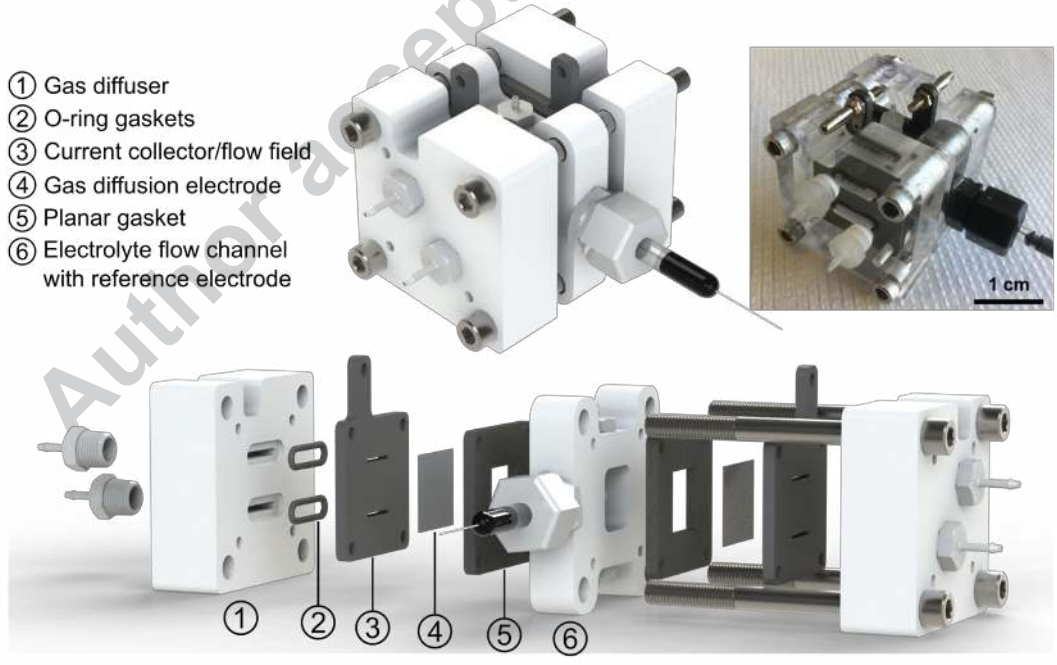

Figure 1. A 3-D computer aided design rendering of the gas-liquid flow reactor. Reactant gases (CO_2 and H_2) are moved in and out of the cell via the (1) gas diffusers. To ensure a gas-tight seal, (2) O-rings are compressed between the diffusers and the graphite current collector/flow fields. Gas diffusion electrodes (4) coated with catalyst (Sn/SnO_2 for the cathode and Pt/C for the anode) are sealed against the current collectors by (5) planar gaskets. Each half cell is assembled identically aside from the GDE catalyst. The (6) electrolyte flow channel with a reference electrode (Ag/AgCl) is placed between the two half-cells and the planar gaskets provide a liquid-tight seal. Liquid is flowed from the bottom to the top of the flow channel. The reactor is compressed by stainless steel bolts and nuts.

2.3 Electrochemical experiments and product quantification

During operation, CO_2 (99.99%, Research Grade 5.0, Airgas) and H_2 (99.9%, Ultra High Purity 5.0, Airgas), were delivered to the cathode and anode, respectively, at a constant flow rate of 10 mL min^{-1} using mass flow controllers (GF40, Brooks Instruments). Hydrogen oxidation to protons on a platinum surface was used as the anodic reaction. The facile kinetics and low electrode potential of this oxidation reaction enable high current operation below the voltage limits of the potentiostat and can simplify subsequent cell analysis, as any performance limitations are expected to come from the slower CO_2 reduction reaction [54]. To ensure hydration of the anodic membrane-electrode interface, the H_2 stream was passed through a water bubbler maintained at 60 °C, via a hotplate (Fisher Scientific), before entering the cell. The CO_2 stream was not hydrated, but used directly from the tank. An aqueous electrolyte solution of 0.5 M Na_2CO_3 (99.999%, Sigma Aldrich) and 0.5 M Na_2SO_4 (99.999%, Sigma Aldrich) dissolved in deionized water (Millipore filtered to 18.2 MΩ), with a pH of 11.36 and 87 mS cm^{-1} (measured

with a Metroohm model # 914 pH/conductivity probe) was passed through the cell using a peristaltic pump (Masterflex L/S Series) at a constant volumetric flow rate of 1 mL min^{-1}. The electrolyte stream was not saturated with CO_2 prior to the experiment. Silicone tubing (Masterflex, L/S 16) was used inside the pump head, while perfluoroalkoxy alkane (PFA) tubing (Swagelok) connected the pump head, reservoir, and flow cell together. All tubing connections were coupled together with PFA or stainless steel compression fittings (Swagelok). To minimize the impact of formate crossover and subsequent re-oxidation on the anode, electrolysis experiments were conducted in single-pass electrolyte mode. Specifically, electrolyte was pumped from a 100 mL reservoir, through the flow cell and into an electrolyte/product collection vessel placed 0.6 m above the cell assembly to ensure a stable gas-liquid pressure balance across the GDEs within the cell, avoiding both gas breakthrough and electrolyte weeping over the course of the experiment. Experiments were performed at room temperature with no temperature measurement and control were not included within the cell. A picture of the experimental setup can be found in the supporting information (Figure S2).

Gaseous products in the effluent gas stream from the cathodic half-cell were injected via an automated sample loop into a gas chromatograph (GC, Agilent 7890). Typically, potentiostatic electrolysis was performed for 1 h. The reported values of faradaic or current efficiency are derived from the average current over 1 h and the average product concentrations of 4-5 GC runs, taken at intervals of 12 min, started 5 min after initiating electrolysis. All electrolysis experiments were repeated three times, for a total of 12-15 GC measurements, and average values are reported herein with associated error bars. Concentrations of the gas phase products (CO and H_2) were found to be stable within ± 5 % during the course of a 1 h electrolysis. Liquid-

phase products were quantified using solvent-suppressed 1D ^{1}H NMR (400 MHz, Bruker Avance) at the end of the electrolysis experiment, as per previously reported procedures [55]. Small amounts of gaseous CO_2 could presumably dissolve in the liquid electrolyte over the course of the experiment resulting in additional minor shifts in pH. However, no such effects were observed in the first 30 min of a typical experiment, before the 1 h electrolysis was started. Currents reported throughout the manuscript are normalized to the cathode geometric area to obtain current densities. All experiments were carried out with an automated voltage correction of 85%, using the real-time current and an internal resistance measurement from potentiostatic electrochemical impedance spectroscopy (EIS) at open-circuit with an amplitude of 5 mV and frequency of 10 kHz. The remaining 15% of the internal resistance contribution to the electrode potential was corrected manually post-run. We did not perform electrolysis with 100% internal resistance correction to minimize current instability due to voltage controller limitations, in accordance with manufacturer recommendations and our own observations with high resistance cells. Typical values of area specific resistance (ASR) measured at open-circuit between the reference electrode and cathode was 2 – 4 Ω cm^2 for both Sn and SnO_2 GDE cathodes. Typical values of ASR for the Nafion coated Pt-GDE anode, also measured from the reference electrode was 8 – 10 Ω cm^2, resulting in a total cell ASR of 10 – 14 Ω cm^2. The cell ASR was measured at open-circuit before and after the electrolysis experiments described below, and exhibited a small increase, typically 5 - 10% of the initial value. Cyclic voltammograms (CVs) were obtained at 50 mV s^{-1} in an aqueous solution of 0.5 M Na_2CO_3 and 0.5 M Na_2SO_4 (pH 11.36).

Micrographs were acquired using a Zeiss Merlin High Resolution Scanning Electron Microscope (SEM), by fixing the samples onto a stainless steel stub (Ted Pella Inc.) with carbon adhesive tabs (Ted Pella Inc.), but without the use of a conductive coating. X-ray diffractograms

(XRD) were obtained using a Rigaku Smartlab instrument with Cu K-α radiation in Bragg-Brentano geometry working at 200 mA and 45 kV, with degree steps of 0.02 and acquisition times of 0.1 s per step.

2.4. Calculation of Efficiencies and Production Rates

We report the current efficiency, voltage efficiency, energy efficiency, and formate production rate in order to effectively compare our experimental results with other systems and to quantitatively compare performance losses. Faradaic or current efficiencies (CE) of each product were calculated by dividing the actual measured product concentration by the theoretical concentration based on the number of coulombs passed during electrolysis. Voltage efficiency (VE) is the ratio of the thermodynamic cell voltage, E^0_{cell}, which is the difference between the anode and cathode half-cell potentials at the reaction conditions, to the experimental cell voltage, E^{exp}_{cell}. Here, we assume that the pH of the cathode is 11.36 across the entire electrode and the pH of the anode is 0 because it remains in contact with an acidic Nafion membrane, in agreement with prior literature [45, 46] . The specific half-cell reactions, (1) and (2), as well as the net reaction (3) are as follows [56-58]:

$$CO_2 + H_2O + 2e^- \rightarrow HCOO^- + OH^- \quad E_{0,C} = -0.896 \text{ V vs. SHE at pH = 11.36} \quad (1)$$

$$2H^+ + 2e^- \rightarrow H_2 \quad E_{0,A} = 0 \text{ V vs. SHE at pH = 0 (Nafion membrane)} \quad (2)$$

$$CO_2 + H_2 \rightarrow HCOO^- + H^+ \quad E_0 = -0.896 \text{ V} \quad (3)$$

Energy efficiency (EE), here, is defined as the product of CE and VE. The average rate of production of formate (mmol m^{-2} s^{-1}) over the course of the 1 h electrolysis was determined by dividing the total amount of formate produced by the experiment duration and geometric area of

the cathode. For the interested reader, a detailed formula and an example calculation for CE, VE, EE, and production rate are provided in the supporting information (Section S.1).

3. Results and Discussion

3.1 *Ex-situ* Characterization and Cyclic Voltammetry

Commercial tin (Sn) and tin oxide (SnO_2) nanoparticles were sprayed onto the MPLs of GDLs to create the GDEs. The Sn and SnO_2 catalyst layers exhibit characteristic gray and off-white colors, respectively, with none of the underlying black GDL visible, indicating complete macroscopic coverage of the sample. SEM images of the same GDEs are shown in Figure S3, where sub-micron structures are evident. Qualitatively, a relatively uniform spherical particle size distribution (100 – 150 nm diameter) was observed for the Sn sample whereas, the SnO_2 sample had a wider size and shape distribution, but generally had particles of 80 – 100 nm diameters. Both observations are in agreement with the manufacturer specification. Furthermore, XRD analysis of the pristine Sn-coated GDE (Figure S4) confirmed the presence of metallic tin with no major oxidation peaks and XRD analysis of the pristine SnO_2-coated GDE sample (Figure S4) confirmed the tin (IV) oxide phase.

The catalyst-coated GDEs were then placed in the electrochemical cell (Figure 1) with a CO_2 (cathode) and H_2 (anode) feed. Figure 2 shows the CVs of the GDEs between -0.3 V and -2.0 V vs. Ag/AgCl conducted at a fixed scan rate of 50 mV s^{-1}. The anodic and cathodic peaks at approximately -0.85 V have been reported previously and been attributed to the formation and reduction of tin oxides in alkaline media [59, 60] . As shown in Figure 2, the SnO_2 GDE exhibited superior catalytic activity as compared to the Sn GDE as evidenced by the larger

current response (both at a comparable area mass loading of 0.35 mg cm^{-2}), which is consistent with several experimental and theoretical studies [29, 32, 61-63]. This has been attributed to the improved binding of CO_2 and its reaction intermediates to the oxygen vacancies present in the oxide-derived material. The inset of Figure 2 shows the differences in the onset potential for appreciable cathodic current in the three systems, defined arbitrarily by a horizontal line at -1 mA cm^{-2} [64, 65]. The bare GDL exhibits an onset potential of -1.46 V vs. Ag/AgCl, which corresponds to H_2 evolution as confirmed by control electrolysis experiments on this sample, where H_2 was the only observable product in the potential range from -1.4 V to -1.7 V vs. Ag/AgCl. The Sn and SnO_2 GDEs exhibit a more anodic onset potential at -1.28 V vs. Ag/AgCl and -1.18 V vs. Ag/AgCl, respectively, which agree with recent literature reports [31, 44].

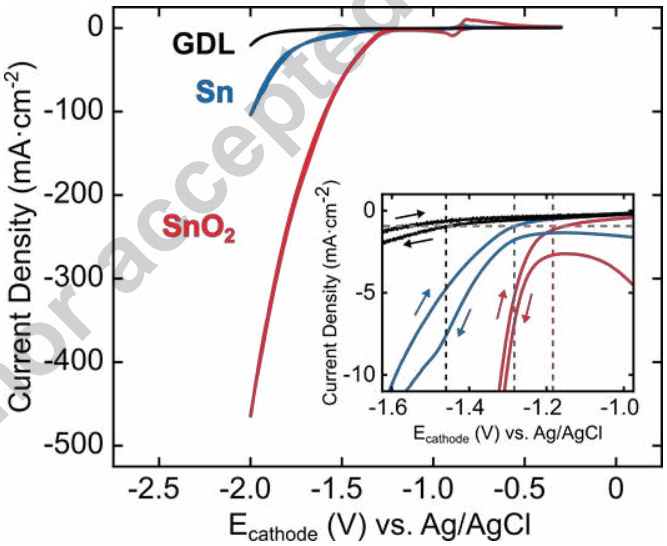

Figure 2. Cyclic voltammograms of a Sn GDE, a SnO_2 GDE, and a bare GDL at 50 mV s^{-1} in an aqueous solution of 0.5 M Na_2CO_3 and 0.5 M Na_2SO_4 (pH 11.36) in the presence of a gaseous CO_2 stream using the flow cell described in Figure 1. Direction of forward and reverse scans are shown by arrows. The initial scan direction is negative. All scans shown are the third scan in a

series of ten, where the fourth and subsequent scans remain stable. No iR correction was performed.

3.2 Electrochemical Reduction of CO_2 at Sn and SnO_2 Gas Diffusion Electrodes

Initially electrolysis experiments using Sn and SnO_2 GDEs were conducted in the flow cell described in Figure 1, with a re-circulating liquid electrolyte from a reservoir of 25 mL. Even at high current densities (> 100 mA cm^{-2}), the formate concentration in these experiments could not be quantified by NMR. This suggests significant crossover through the Nafion membrane due to diffusion and migration leading to re-oxidation of formate to CO_2 at the anode. To circumvent this problem, subsequent electrolysis experiments were conducted using a single pass of the electrolyte to minimize formate re-oxidation; similar approaches have been reported by others [45-47]. While useful for catalyst/electrode analysis, this operating strategy may not be suitable to practical systems as the formate concentration in the effluent stream remains low and a large electrolyte volume is required. Although beyond the scope of the present work, electrolyte recirculation and product separation strategies will need to be developed in the future [66].

Electrolysis experiments were performed on both Sn and SnO_2 GDEs to characterize and compare their activities and stabilities. Figure 3 shows the CE and partial current density results of 1 h potentiostatic electrolysis experiments. Formate ($HCOO^-$), carbon monoxide (CO), and hydrogen (H_2) were detected as products, consistent with previous reports on Sn [21, 45, 52, 56, 67] and SnO_2 [31, 46, 50, 56] catalysts. As expected for both Sn and SnO_2, formate is the major product while H_2 and CO constitute the minor products (< 25% CE) over the potential range from -1.29 V to -1.95 V vs. Ag/AgCl. Figure 3a shows the measured product CEs plotted versus

the iR-corrected cathode potential. The overall mass balance for each constant-potential experiment, indicated by total CE, was closed to within ± 5% (Figure 3a). Partial current densities for each product, calculated by taking the product of CE and current density, are shown in Figure 3b. Representative current density traces versus time (chronoamperograms) for each of the applied cathode potentials experiments are provide in the Supplementary Information (Figure S5).

For Sn GDEs, gaseous H_2 and CO were found to be the minor products from -1.30 V to -1.95 V vs. Ag/AgCl, amounting to less than 25% CE, whereas formate was found to be the major product. At an electrolysis potential of -1.30 V vs. Ag/AgCl (η = 190 mV, where η is the overpotential with respect to the equilibrium potential of the cathodic half-cell reaction in Eqn. (1)), a current density of 2.7 mA cm^{-2} and CE of 70.00 ± 3.99 % to formate was observed. A maximum current density of 214 ± 6 mA cm^{-2} was obtained at a cathodic potential of -1.92 V vs. Ag/AgCl (η = 810 mV) with an associated formate production rate of 7.4 mmol m^{-2} s^{-1} (Figure S6), which is comparable to reported values for Sn-based electrodes (*cf.* Table S1). More negative cathodic potentials were also explored, but the electrolysis current was found to be unstable, possibly due to bubble formation causing resistance fluctuations and interfering with iR compensation at large currents, setting an upper limit for operation in this experimental apparatus. The maximum observed CE for Sn GDEs was 93.76 ± 0.25 % at 83 mA cm^{-2} and -1.71 V vs. Ag/AgCl (η = 600 mV). In addition, 4% CO was also produced at this potential, which corresponds to a total CE of 98% towards CO_2 reduction.

For SnO_2 GDEs, gaseous H_2 and CO were found to be the minor products from -1.29 V to -1.82 V vs. Ag/AgCl, amounting to less than 20% CE, whereas formate was found to be the major product. SnO_2 GDEs exhibited a current density of 12 mA cm^{-2} and CE of 79.00 ± 3.13 % to

formate at a cathodic potential of -1.29 V vs. Ag/AgCl (η = 180 mV). Cathode potentials more positive than -1.29 V were not explored given the relatively small magnitude of the electrolysis current. A maximum current density of 385 ± 19 mA cm^{-2} was obtained at a cathodic potential of -1.82 V vs. Ag/AgCl (η = 710 mV) with an associated rate of formate production (Figure S6) of 14.9 mmol m^{-2} s^{-1}, which is among the highest values reported for Sn-based electrodes to date (*cf.* Table S1). More negative cathodic potentials were also explored, but the electrolysis current was found to be unstable due to electrolyte flooding of the GDE. Although the peak CE for Sn is larger (93.76 ± 0.25 %) than for SnO_2 (90.00 ± 0.69 % at -1.65 V vs. Ag/AgCl (η = 540 mV) and 110 mA cm^{-2}), the SnO_2 GDEs exhibit high selectivity to formate over a wider range of applied potentials. In addition, 7% CO was produced at the peak formate potential for SnO_2, which corresponds to a total CE of 97% towards CO_2 reduction.

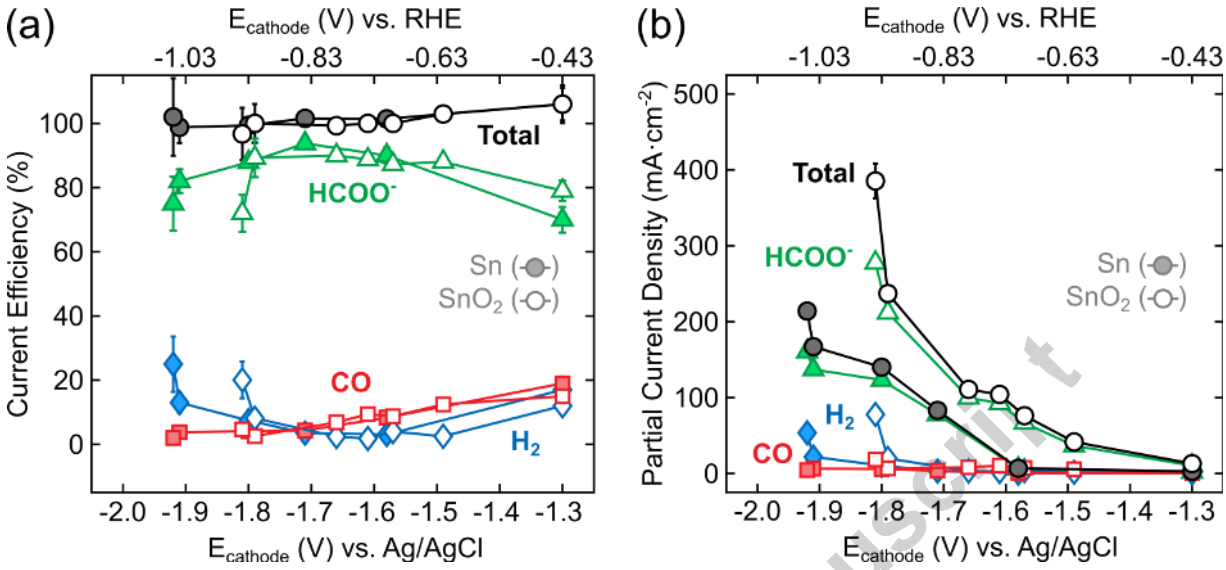

Figure 3. Plots of current efficiency (a) and partial current density (b) as a function of iR-corrected applied cathodic potential for Sn and SnO_2 GDEs for a 1 h electrolysis experiment. Partial current density is calculated by taking the product of measured current density and current efficiency at each potential. Error bars are the average of three electrolysis experiments, each of which uses the average of 4-5 GC analyses to measure CO and H_2 concentration. Some error bars are too small to resolve.

Plots of iR-corrected cathode potential (Figure S7) and cell voltage (Figure S8) versus the measured current density can be found in the supporting information. The measured CE (Figure 3a) and cell voltages (Figure S8) from the electrolysis experiments were used to calculate the energy efficiency (EE) of the electrochemical cell for each catalyst (Figure S9). EE ranged from 29 ± 3.33 % (-1.92 V vs. Ag/AgCl) to 63 ± 3.62 % (-1.30 V vs. Ag/AgCl) for cells with Sn GDEs and from 26.11 ± 5.75% (-1.82 V vs. Ag/AgCl) 68.06 ± 3.13 % (-1.29 V vs. Ag/AgCl) for cells with SnO_2 GDEs.

Based on the variation in current density over the course of 1 h (Figure S5) electrolysis experiments, it is evident that the Sn GDEs become increasingly active. This phenomenon is typically attributed to a gradual wetting of the electrode surface which increases access to catalyst sites, which agrees with prior Sn-GDE literature [19, 35]. In contrast, the current densities for SnO_2 GDEs initially increase over the first 10 min, and subsequently stabilize at a lower current density (Figure S5). We hypothesize that this behavior is due to the electrochemical reduction of the metal oxide to the metal, as will be further discussed in Section 3.4, but it also suggests that the initial SnO_2 catalyst layer wets more completely than the Sn catalyst layer, potentially due to its polar heteroatom and oxophilic composition [68]. An exception for SnO_2 occurred at the highest reported potential where the current density increased throughout the experiments.

In considering the source of the improved electrode performance, it is necessary to differentiate changes in electrochemical surface area from improvements in kinetic rates. As previously reported in literature [31] and qualitatively confirmed here via BET measurements, the gravimetric surface area of the SnO_2 nanopowders (23 m^2 g^{-1}) is more than two times greater than that of the Sn powder (9.5 m^2 g^{-1}). This is partially attributable to the smaller particle size of SnO_2 (90 nm) as compared to Sn (125 nm, see Figure S3). However, Lee *et al.* have shown that the SnO_2 nanoparticles demonstrate electrocatalytic performance superior to Sn even when they are annealed to achieve a comparable gravimetric surface area (6.2 m^2 g^{-1}) [31]. Moreover, both catalysts exhibit a similar morphology and particle size after electrolysis, as demonstrated in this study (*cf.* Figure 5). Thus, we attribute the superior performance of the SnO_2 GDE to the inherent electrocatalytic activity of the oxide-derived material and not the difference in surface area, consistent with prior studies [31].

Using data from the CV and electrolysis experiments (Figures 2-3), we generated and analyzed Tafel plots for both GDEs (Figure S10) and performed linear fits in both a high and low overpotential region to quantify the Tafel slope as a measure of catalyst activity. Note that a lower value for Tafel slope corresponds to a greater increase in catalyst activity per unit increase in cathode overpotential. At low overpotentials ($\eta < 0.5$ V), Sn and SnO_2 GDEs exhibit a slope of 105 mV decade^{-1} and 38 mV decade^{-1} respectively, consistent with previous literature reports [62]. Electrochemical kinetic studies for the reduction of CO_2 to formate over Sn and SnO_2 electrodes have been reported and vary widely in the Tafel slopes from 70 to 480 mV decade^{-1} [21, 23, 26, 29, 30, 59, 62, 69]. At higher overpotentials ($\eta > 0.5$ V), Sn and SnO_2 GDEs exhibit a slope of 302 mV decade^{-1} and 176 mV decade^{-1} respectively (*cf.* Figure S10), which are again comparable to previous literature reports of CO_2 reduction using gas-phase delivery [11, 59]. The origin of such Tafel behavior is not well understood but has been hypothesized as either mass transfer effects or alternate reaction mechanisms and rate-determining steps [21, 26]. Since ohmic contributions are removed from these measurements, via iR correction, the observed polarization is attributed to the combined charge and mass transfer resistance of the cathodic half-cell reaction. Given the complexity of the various contributions, these analyses are restricted to a simple comparison of the Sn and SnO_2 nanomaterials in the current electrolyzer configuration. A better understanding of mass transfer resistance and associated limiting currents for CO_2 reduction in a gas-phase electrolyzer design are required and will be the subject of future investigation.

3.3 Post-Electrolysis Analysis

After the electrolysis experiments shown in Figure 3 were conducted, the electrodes were analyzed by XRD and SEM measurements. The XRD pattern of Sn GDEs remained largely unaffected, but small oxide peaks were observed, likely due to surface oxidation in air after the sample was removed from the electrochemical cell. Figure 4 shows the XRD patterns of two different SnO_2 GDEs after electrolysis at -1.49 V vs. Ag/AgCl (-0.62 V vs. RHE) and -1.29 V vs. Ag/AgCl (-0.42 V vs. RHE) respectively. As described earlier, recent studies by Lee *et al*., using a liquid-phase CO_2 delivery system, demonstrated that by choosing a potential-pH combination of -0.6 V vs. RHE and pH 10-12, the SnO_2 phase could be maintained over a 5 h electrolysis experiment of CO_2 reduction to formate [31]. We observe similar behavior in this study, using a gas-phase CO_2 delivery system. Across all experiments, the electrolyte pH remains within the optimal stability range for SnO_2, confined to a maximum decrease from 11.3 to 10.7 over the course of an electrolysis run, where the reduced alkalinity is likely associated with proton generation at the anode, but could also be due to carbonation from the CO_2. At an applied potential of -0.42 V vs. RHE, the post-electrolysis XRD pattern (see Figure 4) exhibited clear and distinct peaks for SnO_2 and none for metallic Sn, indicating that the oxide phase was retained during the electrolysis. At an applied potential of -0.62 V vs. RHE, post-electrolysis analysis revealed that characteristic peaks of SnO_2, at 34° and 38°, disappeared and those characteristic to Sn, at 30° and 32°, are clearly observed after electrolysis, indicating the reduction of SnO_2 to metallic Sn [7]. The sample also changed color from off-white to grey providing further evidence of oxide reduction to metal (*cf.* Figure S3). Minor peaks from the tin (IV) oxide were also observed, either due to residual oxide content or re-oxidation in air post-

experiment. The peaks labeled with a red asterisk do not correspond to any peak in the diffraction pattern of either bare GDL, Sn, or SnO_2, and are designated to be an unknown crystalline impurity that is also present in the pristine sample (see Figure S4). While these impurity peaks were not identified, our results show that they are persistent on the timescale of our experiments with no change in their shape or intensity after electrolysis was completed at both -0.42 V RHE and -0.62 V RHE. Hence, these impurities do not affect the major conclusions of this study, which are in agreement with observations in the prior literature. While the oxide phase can be successfully retained by balancing potential and pH, the associated current density (12 mA cm^{-2}) is likely too low for practical application [33, 70-72]. Consequently, the use of oxide-derived materials in conjunction with pH and potential control is likely to pose a challenge for realizing both high performance and durability in industrial scale systems.

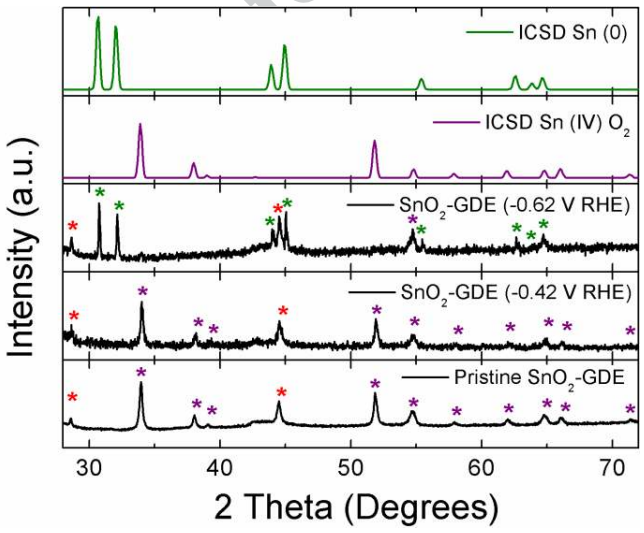

Figure 4. XRD analysis of pristine SnO_2 GDEs, after electrolysis at -0.62 V vs. RHE and -0.42 V vs. RHE. Database standards for Sn, SnO, and SnO_2 included for comparison. Peaks marked in red asterisk do not correspond to any peaks in the diffraction pattern of either bare GDL, Sn or SnO_2, and are designated to be some unknown crystalline impurity in the pristine sample.

Finally, both GDEs were analyzed post-electrolysis using SEM, as shown in Figure 5. The Sn nanoparticles (Figure 5a) were found to agglomerate forming irregularly sized micron-scale clusters in the catalyst layer. The SnO_2 GDE (Figure 5c) exhibited a similar fused structure of micron-sized aggregates, suggesting a gradual loss of accessible electrochemically active surface area [73]. This result is in contrast to recent studies by Zhou *et al*., where 100 nm Sn particles were observed to progressively decrease in size over the course of a 60 h electrolysis experiment at a modest current density (<< 100 mA cm^{-2}), which the authors attributed to a hydrogen diffusion induced stress mechanism [74]. Given the difference in test durations, further long-term studies of these Sn and SnO_2 GDEs at variable current densities would be required to determine if such pulverization behavior occurs. This will be the subject of future investigation. Figure 5d also shows the elemental map through energy dispersive X-ray analysis at the Sn-L edge, demonstrating that a significant amount of the carbonaceous GDL underneath the catalyst layer was now exposed (46% carbon as estimated from the pixel count) as compared to the pristine catalyst-coated GDEs. Further, the relative distribution of catalyst on the GDE after electrolysis was not consistent across the electrode. The small cross section (40 µm × 30 µm) shown in Figure 5d represents the most extreme case of catalyst erosion observed on the sample. A wider cross section of the same sample is shown in Figure S11. Previous reports on Sn-based catalysts in liquid-phase systems have noted catalyst degradation and erosion from the electrode surface resulting from cathodic corrosion [75, 76], but similar issues have yet to be reported in gas-phase systems that leverage GDEs [45, 46]. In addition to previous reports of corrosion-induced pathways [75, 76], local variations in the gas-liquid pressure balance, and resulting bubble formation or liquid penetration, as well as the shear stress imparted by the flowing electrolyte stream, may exacerbate catalyst erosion rates. Such effects are expected to be pronounced in this

study due to the relatively low initial catalyst loading (0.35 mg cm^{-2}), as compared to recent reports in a similar cell configuration that utilized considerably higher catalyst loadings (> 5 mg cm^{-2}) [45, 46], but nevertheless occur and represent a challenge to the long term electrode performance.

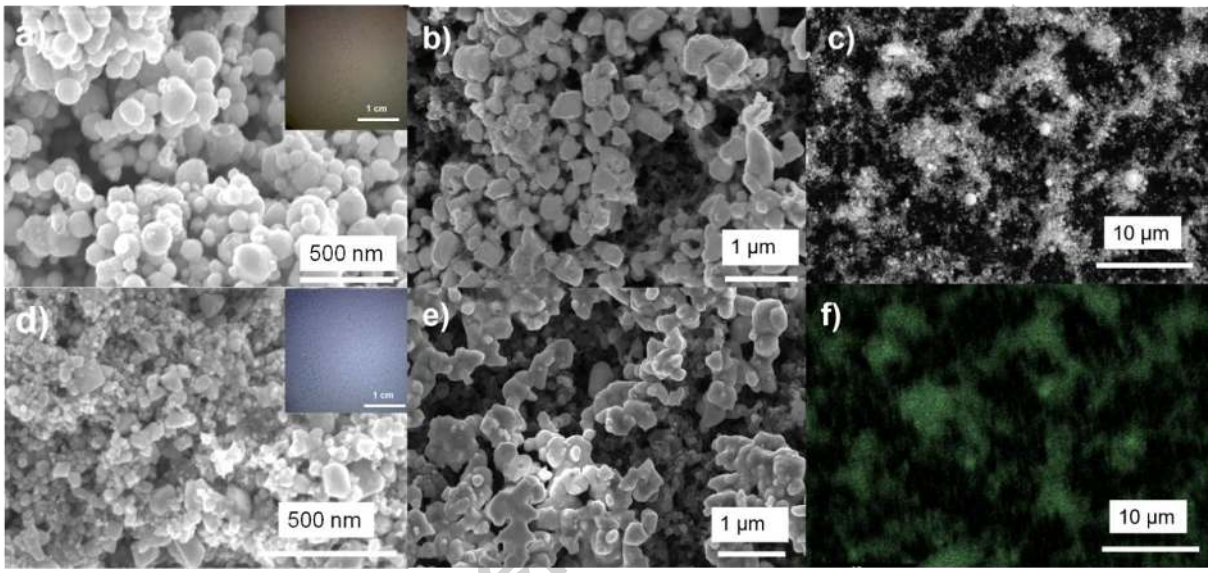

Figure 5. Representative SEM images of Sn (a) spray coated on the surface of a GDL (inset shows optical image), (b) after a 1 h electrolysis at -1.6 V vs. Ag/AgCl, (d, e) are corresponding images for SnO_2, (c, f) EDX maps of the image shown in (b) at the Sn-L edge

Conclusions

We investigate the performance and durability of Sn and SnO_2 GDEs for the electroreduction of CO_2 to formate in a gas-fed flow reactor with an integrated reference electrode that enables single electrode characterization at high current densities. We find that, over the course of a 1 h electrolysis, both electrodes retain high selectivity (> 70%) for the desired product at current

densities in excess of 200 mA cm^{-2} at catalyst loadings of 0.35 mg cm^{-2}, and that the SnO_2 GDEs outperform the Sn GDEs due to enhanced reaction kinetics. Peak CEs of 93.76 ± 0.25 % and 90.00 ± 0.69 % are observed for Sn and SnO_2, respectively, although SnO_2 experiences a broader potential range for high formate CE. Due to the low catalyst loadings, the mass activities demonstrated in this study are among the highest reported to date. Further improvements in electrode performance may be achieved through systematic analyses of catalyst loading, ink composition, electrode substrate, and deposition strategy, carefully balancing considerations of cost, catalytic performance and ease of fabrication. However, both electrodes experience significant changes after high current operation including reduction of the metal oxide to metal at cathode potentials more negative than -0.6 V vs. Ag/AgCl, nanoparticle agglomeration, and catalyst layer erosion. Understanding and mitigating these decay processes is key to extending electrode lifetime without sacrificing formate generation rates or process efficiency.

Acknowledgements

This work made use of the MRSEC Shared Experimental Facilities at MIT, supported by the National Science Foundation under award number DMR-1419807. The authors acknowledge the financial support of DOE SBIR Contract #DE-SC0015173. The authors thank Michael Orella of the Brushett Research Group for insightful discussions and assistance with experiments.

Appendix A. Supplementary data

Supplementary data related to this article can be found at https://doi.org/xxx.

References

1. Schiffer, Z.J. and K. Manthiram, (2017), Electrification and Decarbonization of the Chemical Industry. Joule,. 1(1): p. 10-14.
2. Chen, A. and B.-L. Lin, (2018), A Simple Framework for Quantifying Electrochemical CO_2 Fixation. Joule,. 2(4): p. 594-606.
3. Lechtenböhmer, S., et al., (2016), Decarbonising the energy intensive basic materials industry through electrification – Implications for future EU electricity demand. Energy, 115: p. 1623-1631.
4. Centi, G., E.A. Quadrelli, and S. Perathoner, (2013), Catalysis for CO_2 conversion: a key technology for rapid introduction of renewable energy in the value chain of chemical industries. Energy & Environmental Science,. 6(6): p. 1711-1731.
5. Koytsoumpa, E.I., C. Bergins, and E. Kakaras, (2018),The CO_2 economy: Review of CO_2 capture and reuse technologies. The Journal of Supercritical Fluids,. 132: p. 3-16.
6. Zhang, W., et al., (2018.), Progress and Perspective of Electrocatalytic CO_2 Reduction for Renewable Carbonaceous Fuels and Chemicals. Advanced Science, 5(1): p. 1700275.
7. Lu, Q. and F. Jiao (2016), Electrochemical CO_2 reduction: Electrocatalyst, reaction mechanism, and process engineering. Nano Energy, 29: p. 439-456.
8. Kumar, B., et al., (2016.) New trends in the development of heterogeneous catalysts for electrochemical CO_2 reduction. Catalysis Today, 270: p. 19-30.
9. Dutta, A., et al., (2018), Beyond Copper in CO_2 Electrolysis: Effective Hydrocarbon Production on Silver Nano-Foam Catalysts. ACS Catalysis,.
10. Dutta, A., et al., (2017) Electrochemical CO_2 Conversion Using Skeleton (Sponge) Type of Cu Catalysts. ACS Catalysis,. 7(8): p. 5431-5437.
11. Wang, Q., H. Dong, and H. Yu, (2014) Development of rolling tin gas diffusion electrode for carbon dioxide electrochemical reduction to produce formate in aqueous electrolyte. Journal of Power Sources, 271: p. 278-284.
12. Wang, Q., et al., (2015) Enhanced performance of gas diffusion electrode for electrochemical reduction of carbon dioxide to formate by adding polytetrafluoroethylene into catalyst layer. Journal of Power Sources, 279: p. 1-5.
13. Pérez-Rodríguez, S., et al., (2016) Electrochemical reactors for CO_2 reduction: From acid media to gas phase. International Journal of Hydrogen Energy, 41(43): p. 19756-19765.
14. Lu, X., et al., (2017) A high performance dual electrolyte microfluidic reactor for the utilization of CO_2. Applied Energy,. 194: p. 549-559.
15. Merino-Garcia, I., et al., (2016) Electrochemical membrane reactors for the utilisation of carbon dioxide. Chemical Engineering Journal, 305: p. 104-120.

16. Hori, Y., et al., (1994) Electrocatalytic process of CO selectivity in electrochemical reduction of CO_2 at metal electrodes in aqueous media. Electrochimica Acta, 39(11): p. 1833-1839.
17. Wang, Y., C. Niu, and D. Wang, (2018) Metallic nanocatalysts for electrochemical CO_2 reduction in aqueous solutions. Journal of Colloid and Interface Science, 527: p. 95-106.
18. Agarwal, A.S., et al., (2011) The Electrochemical Reduction of Carbon Dioxide to Formate/Formic Acid: Engineering and Economic Feasibility. ChemSusChem, 4(9): p. 1301-1310.
19. Garron, A. and F. Epron, (2005) Use of formic acid as reducing agent for application in catalytic reduction of nitrate in water. Water Research, 39(13): p. 3073-3081.
20. Muck, R.E., et al., (2018) Silage review: Recent advances and future uses of silage additives. Journal of Dairy Science, 101(5): p. 3980-4000.
21. Chen, Y. and M.W. Kanan, (2012) Tin Oxide Dependence of the CO_2 Reduction Efficiency on Tin Electrodes and Enhanced Activity for Tin/Tin Oxide Thin-Film Catalysts. Journal of the American Chemical Society, 134(4): p. 1986-1989.
22. Wu, J., et al., (2012) Electrochemical Reduction of Carbon Dioxide I. Effects of the Electrolyte on the Selectivity and Activity with Sn Electrode. Journal of The Electrochemical Society, 159(7): p. F353-F359.
23. Wu, J., et al., (2014) Electrochemical reduction of carbon dioxide III. The role of oxide layer thickness on the performance of Sn electrode in a full electrochemical cell. Journal of Materials Chemistry A, 2(6): p. 1647-1651.
24. Wu, J., et al., (2013) Electrochemical Reduction of Carbon Dioxide: II. Design, Assembly, and Performance of Low Temperature Full Electrochemical Cells. Journal of The Electrochemical Society, 160(9): p. F953-F957.
25. Wu, J., et al., (2014) Electrochemical reduction of carbon dioxide: IV dependence of the Faradaic efficiency and current density on the microstructure and thickness of tin electrode. Journal of Power Sources, 258: p. 189-194.
26. Zhang, S., P. Kang, and T.J. Meyer, (2014) Nanostructured Tin Catalysts for Selective Electrochemical Reduction of Carbon Dioxide to Formate. Journal of the American Chemical Society, 136(5): p. 1734-1737.
27. Bashir, S., et al., (2016) Electrocatalytic reduction of carbon dioxide on SnO_2/MWCNT in aqueous electrolyte solution. Journal of CO_2 Utilization, 16: p. 346-353.
28. Fu, Y., et al., (2016) Electrochemical CO_2 reduction to formic acid on crystalline SnO2 nanosphere catalyst with high selectivity and stability. Chinese Journal of Catalysis, 37(7): p. 1081-1088.
29. Kumar, B., et al., (2017) Reduced SnO_2 Porous Nanowires with a High Density of Grain Boundaries as Catalysts for Efficient Electrochemical CO_2-into-HCOOH Conversion. Angewandte Chemie International Edition, 56(13): p. 3645-3649.
30. Li, F., et al., (2017) Hierarchical Mesoporous SnO_2 Nanosheets on Carbon Cloth: A Robust and Flexible Electrocatalyst for CO_2 Reduction with High Efficiency and Selectivity. Angewandte Chemie International Edition,. 56(2): p. 505-509.
31. Lee, S., et al., (2015) Alkaline CO_2 Electrolysis toward Selective and Continuous HCOO– Production over SnO_2 Nanocatalysts. The Journal of Physical Chemistry C, 119(9): p. 4884-4890.

32. Eilert, A., et al., (2017) Subsurface Oxygen in Oxide-Derived Copper Electrocatalysts for Carbon Dioxide Reduction. The Journal of Physical Chemistry Letters, 8(1): p. 285-290.
33. Pletcher, D., (2015) The cathodic reduction of carbon dioxide—What can it realistically achieve? A mini review. Electrochemistry Communications, 61: p. 97-101.
34. Paidar, M., V. Fateev, and K. Bouzek, (2016) Membrane electrolysis—History, current status and perspective. Electrochimica Acta, 209: p. 737-756.
35. Wiebe, R. and V.L. Gaddy, (1940) The Solubility of Carbon Dioxide in Water at Various Temperatures from 12 to 40° and at Pressures to 500 Atmospheres. Critical Phenomena*. Journal of the American Chemical Society,. 62(4): p. 815-817.
36. John R. Rumble, ed., CRC Handbook of Chemistry and Physics, 99th Edition (Internet Version 2018), CRC Press/Taylor & Francis, Boca Raton, FL.
37. Proietto, F., et al., (2018) Electrochemical conversion of CO_2 to HCOOH at tin cathode in a pressurized undivided filter-press cell. Electrochimica Acta, 277: p. 30-40.
38. Scialdone, O., et al., (2016) Electrochemical reduction of carbon dioxide to formic acid at a tin cathode in divided and undivided cells: effect of carbon dioxide pressure and other operating parameters. Electrochimica Acta, 199: p. 332-341.
39. Hashiba, H., et al., (2016) Systematic Analysis of Electrochemical CO_2 Reduction with Various Reaction Parameters using Combinatorial Reactors. ACS Combinatorial Science, 18(4): p. 203-208.
40. Endrődi, B., et al., (2017) Continuous-flow electroreduction of carbon dioxide. Progress in Energy and Combustion Science, 62: p. 133-154.
41. Delacourt, C., et al., (2008) Design of an Electrochemical Cell Making Syngas ($CO + H_2$) from CO_2 and H_2O Reduction at Room Temperature. Journal of The Electrochemical Society, 155(1): p. B42-B49.
42. Jhong, H.-R.M., F.R. Brushett, and P.J.A. Kenis, (2013) The Effects of Catalyst Layer Deposition Methodology on Electrode Performance. Advanced Energy Materials, 3(5): p. 589-599.
43. Ma, S., et al., (2016) One-step electrosynthesis of ethylene and ethanol from CO_2 in an alkaline electrolyzer. Journal of Power Sources,. 301: p. 219-228.
44. Del Castillo, A., et al., (2015) Electrocatalytic reduction of CO_2 to formate using particulate Sn electrodes: Effect of metal loading and particle size. Applied Energy, 157: p. 165-173.
45. Kopljar, D., et al., (2014) Electrochemical reduction of CO2 to formate at high current density using gas diffusion electrodes. Journal of Applied Electrochemistry, 44(10): p. 1107-1116.
46. Kopljar, D., N. Wagner, and E. Klemm, (2016) Transferring Electrochemical CO2 Reduction from Semi-Batch into Continuous Operation Mode Using Gas Diffusion Electrodes. Chemical Engineering & Technology, 39(11): p. 2042-2050.
47. Yang, H., et al., (2017) Electrochemical conversion of CO_2 to formic acid utilizing Sustainion™ membranes. Journal of CO_2 Utilization, 20: p. 208-217.
48. Kutz, R.B., et al., (2017) Sustainion Imidazolium-Functionalized Polymers for Carbon Dioxide Electrolysis. Energy Technology, 5, 6, 929- 936
49. Sen, S., et al., (2016) Pulsed Electrodeposition of Tin Electrocatalysts onto Gas Diffusion Layers for Carbon Dioxide Reduction to Formate. MRS Advances, 2(8): p. 451-458.

50. Irtem, E., et al., (2016) Low-energy formate production from CO_2 electroreduction using electrodeposited tin on GDE. Journal of Materials Chemistry A, 4(35): p. 13582-13588.
51. Del Castillo, A., M. Alvarez-Guerra, and A. Irabien, (2014) Continuous electroreduction of CO_2 to formate using Sn gas diffusion electrodes. AIChE Journal, 60(10): p. 3557-3564.
52. Del Castillo, A., et al., (2017) Sn nanoparticles on gas diffusion electrodes: Synthesis, characterization and use for continuous CO_2 electroreduction to formate. Journal of CO_2 Utilization, 18: p. 222-228.
53. Milshtein, J.D., et al., (2016) High current density, long duration cycling of soluble organic active species for non-aqueous redox flow batteries. Energy & Environmental Science, 9(11): p. 3531-3543.
54. Rheinländer, P.J., et al., (2014) Kinetics of the Hydrogen Oxidation/Evolution Reaction on Polycrystalline Platinum in Alkaline Electrolyte Reaction Order with Respect to Hydrogen Pressure. Journal of The Electrochemical Society, 161(14): p. F1448-F1457.
55. Sen, S., D. Liu, and G.T.R. Palmore, (2014) Electrochemical Reduction of CO_2 at Copper Nanofoams. ACS Catalysis, 4(9): p. 3091-3095.
56. Li, H. and C. Oloman, (2005) The Electro-Reduction of Carbon Dioxide in a Continuous Reactor. Journal of Applied Electrochemistry, 35(10): p. 955-965.
57. Li, H. and C. Oloman, (2006) Development of a continuous reactor for the electro-reduction of carbon dioxideto formate – Part 1: Process variables. Journal of Applied Electrochemistry, 36(10): p. 1105.
58. Li, H. and C. Oloman, (2007) Development of a continuous reactor for the electro-reduction of carbon dioxide to formate – Part 2: Scale-up. Journal of Applied Electrochemistry, 37(10): p. 1107-1117.
59. Prakash, G.K.S., F.A. Viva, and G.A. Olah, (2013) Electrochemical reduction of CO_2 over Sn-Nafion® coated electrode for a fuel-cell-like device. Journal of Power Sources, 223: p. 68-73.
60. Kapusta, S.D. and N. Hackerman, (1980) Anodic passivation of tin in slightly alkaline solutions. Electrochimica Acta, 25(12): p. 1625-1639.
61. Saravanan, K., et al., (2017) Computational investigation of CO_2 electroreduction on tin oxide and predictions of Ti, V, Nb and Zr dopants for improved catalysis. Journal of Materials Chemistry A, 5, 11756 - 11763
62. Lee, C.W., et al., (2017) Reaction Mechanisms of the Electrochemical Conversion of Carbon Dioxide to Formic Acid on Tin Oxide Electrodes. ChemElectroChem, 4, 9, 2130 -2136
63. Cui, C., et al., (2016) Promotional effect of surface hydroxyls on electrochemical reduction of CO_2 over SnOx/Sn electrode. Journal of Catalysis, 343: p. 257-265.
64. Benck, J.D., et al., (2014) Substrate Selection for Fundamental Studies of Electrocatalysts and Photoelectrodes: Inert Potential Windows in Acidic, Neutral, and Basic Electrolyte. PLOS ONE, 9(10): p. e107942.
65. Anantharaj, S., et al., (2018) Precision and correctness in the evaluation of electrocatalytic water splitting: revisiting activity parameters with a critical assessment. Energy & Environmental Science, 11, 744 - 771
66. Greenblatt, J.B., et al., (2018) The Technical and Energetic Challenges of Separating (Photo)Electrochemical Carbon Dioxide Reduction Products. Joule, 2(3): p. 381-420.

67. Brushett, F.R., et al., (2016) Development of Novel Tin Nanostructures Using Pulse Plating Methods for the Electroreduction of Carbon Dioxide to Formic Acid. Meeting Abstracts, MA2016-02(40): p. 3012.
68. Masuda, Y., T. Ohji, and K. Kato, (2012) Tin Oxide Nanosheet Assembly for Hydrophobic/Hydrophilic Coating and Cancer Sensing. ACS Applied Materials & Interfaces, 4(3): p. 1666-1674.
69. Won, D.H., et al., (2015) Rational Design of a Hierarchical Tin Dendrite Electrode for Efficient Electrochemical Reduction of CO_2. ChemSusChem, 8(18): p. 3092-3098.
70. Liu, Z., et al., (2016) Electrochemical generation of syngas from water and carbon dioxide at industrially important rates. Journal of CO_2 Utilization, 15: p. 50-56.
71. Verma, S., et al., (2016) A Gross-Margin Model for Defining Technoeconomic Benchmarks in the Electroreduction of CO_2. ChemSusChem, 9(15): p. 1972-1979.
72. Jouny, M., W. Luc, and F. Jiao, (2018) General Techno-Economic Analysis of CO_2 Electrolysis Systems. Industrial & Engineering Chemistry Research, 57(6): p. 2165-2177.
73. Manthiram, K., B.J. Beberwyck, and A.P. Alivisatos, (2014) Enhanced Electrochemical Methanation of Carbon Dioxide with a Dispersible Nanoscale Copper Catalyst. Journal of the American Chemical Society, 136(38): p. 13319-13325.
74. Wu, J., S.-G. Sun, and X.-D. Zhou, (2016) Origin of the performance degradation and implementation of stable tin electrodes for the conversion of CO_2 to fuels. Nano Energy, 27: p. 225-229.
75. Anawati, et al., (2014) Degradation and deactivation of Sn catalyst used for CO_2 reduction as function of overpotential. Electrochimica Acta, 133: p. 188-196.
76. Salzberg, H.W. and F. Mies, (1958 Cathodic Disintegration of Tin. Journal of The Electrochemical Society, 105(2): p. 64-66.

Graphical Abstract